J Solid State Electrochem (2013) 17:145–156
DOI 10.1007/s10008-012-1857-6

ORIGINAL PAPER

Oxidation of electrodeposited cobalt electrodes in an alkaline electrolyte

M. Grdeń · J. Jagiełło

Received: 9 June 2012 / Revised: 9 August 2012 / Accepted: 28 August 2012 / Published online: 18 September 2012

Abstract The oxidation of electrodeposited Co electrodes has been studied in 0.1 M KOH_{aq} at potentials more negative than −880 mV vs. Hg|HgO by means of electrochemical quartz crystal microbalance (EQCM) and rotating ring disk electrode coupled with cyclic voltammetry (CV) and chronoamperometry (CA). Dissolution of cobalt was found to be insignificant and does not constitute a step in the overall process of formation of the oxidised layer. The irreversibility of the oxidation process depends on the electrode potential and oxidation time. The composition of the oxidised layer depends on the oxidation potential: $Co(OH)_2$ is formed at more negative potentials, while at more positive potentials CoO is the prevailing product. The results obtained by means of three techniques (CV, CA and EQCM) reveal that at potentials not higher than −880 mV, the oxidation of Co follows a direct logarithmic law. The mechanism of the process is discussed.

Keywords Cobalt · Electrochemical quartz crystal microbalance (EQCM) · Metal oxidation

Introduction

Recent experiments conducted on noble metal electrodes [1–3] show that the process of surface electrooxidation can be divided into two basic steps: (1) the early stages of formation of the oxidised layer up to ca. one monolayer and (2) further thickening of the oxidised layer. Each of these stages proceeds according to a different mechanism. It was found that the early stages of electrochemical formation of a surface oxide/hydroxide of noble [1–6] and some of non-noble metals [7] can be described by the direct logarithmic law. This law predicts a linear relationship between the amount of the oxidised layer formed, in thickness or charge units, and the logarithm from the oxidation time. The origin of the direct logarithmic law was discussed in the literature and respective mathematical models have been derived [4, 6, 8]. These models, however, have not been applied widely and were used for the analysis of only a few electrochemical systems. Full understanding of the problem requires extension of kinetic studies to non-noble electrodes. Interestingly, the direct logarithmic law is applicable also for non-electrochemical oxidation of metals [9–11], e.g. cobalt [12].

The process of oxidation of noble metals is usually reversible [1–5], and their solubility in various aqueous media is very often insignificant [13, 14]. For these metals, the amount of the oxidised layer formed can be easily determined from the measurements of charge of its reduction. The situation becomes more complex for non-noble metals due to the irreversibility of the oxidation process, i.e. formation of hardly reducible layers, and often significant contribution from dissolution of the electrode material. Lack of reliable methods of real surface area determination for many of non-noble metals further complicates the studies.

Cobalt has been selected as a subject of studies on the applicability of direct logarithmic law for oxidation of non-noble electrodes. The surface of Co can be easily oxidised when in contact with moisture or air [12, 15]. Despite its numerous applications [16–19], the mechanism of the early stages of Co oxidation in aqueous alkaline solutions has not been studied extensively. Most works focus instead on the composition of Co oxidation products. For potentials more negative than −500 mV vs. Hg|HgO, the proposed products include CoO [20–24], hydrated CoO [25] or various forms of $Co(OH)_2$ [20–24, 26–32].

M. Grdeń (✉) · J. Jagiełło
Faculty of Chemistry, University of Warsaw,
Pasteura 1,
02-093 Warsaw, Poland
e-mail: mgrden@chem.uw.edu.pl

An analysis of polarisation curves for Co oxidation in 1 M NaOH reveals that the process follows nucleation and growth mechanism with transfer of the first electron as the rate-determining step [31]. In [33], Co oxidation at potentials more negative than −330 mV vs. Ag|AgCl was studied in 0.1 and 1 M NaOH by means of rotating ring disk electrode (RRDE), scanning electrochemical microscopy and atomic force microscopy. Although some dissolution of the electrode was detected, it was concluded that Co oxidation is predominated by a solid state reaction. It was also pointed out that the oxidised layer is formed in a 3D scheme rather than in a layer-by-layer manner. On the other hand, formation of 2D structures during early stages of oxidation of Co single crystals in 0.1 M NaOH was reported in [29] on the basis of STM measurements. A solid state pathway of formation of Co(II) layer was also proposed in [22] for 0.2–8 M KOH with dissolution predominantly of $Co(OH)_2$ rather than metallic cobalt.

Cobalt dissolution is observed in alkaline solutions at potentials as negative as −850 mV vs. Hg|HgO [20, 22, 23, 33–37] and depends on pH [20]. It is not clear, however, whether the dissolution is a step in the overall process of Co (II) layer formation or a side reaction only [22, 25, 33]. Further complications in studies of Co oxidation are related to the irreversibility of the process caused by an extended Co dissolution or by the formation of a hardly reducible oxidised layer [23, 34–36]. Such irreversibility complicates the application of Co oxidation charges in determination of the real surface area [38], as was already discussed in [34].

In this paper, we report the results of studies on early stages of oxidation of electrodeposited cobalt electrode to Co(II) compounds in 0.1 M KOH_{aq}. The necessity of application of methods allowing the evaluation of Co solubility (RRDE), reversibility of oxidation process and simultaneous determination of mass changes (electrochemical quartz crystal microbalance, EQCM) leads to selection of electrodeposited Co layers as subject of the studies rather than massive cobalt. The mechanism of the process was evaluated on the basis of chronoamperometric, cyclic voltammetry and EQCM results. We focused on potential range where thin oxidised layers with thickness below the monolayer are formed. The composition of the oxidised layer was determined on the basis of EQCM and X-ray photoelectron spectroscopy results.

Experimental

Co electrodes were prepared by constant potential electrodeposition (−805 mV) from a bath containing 0.6 M $CoSO_4 \cdot 7H_2O$ (POCh, p.a.), 0.3 M KCl (Chempur, p.a.) and 0.26 M H_3BO_3 (POCh, p.a.) [34], with a Co wire (Johnson Matthey, 99.999 %) and Ag|AgCl serving as a counter and as a reference electrode, respectively. Various substrates were used for electrodeposition: Au wire or foil (99.9 %, Mint of Poland, in CV and X-ray photoelectron spectroscopy (XPS) measurements), gold-covered quartz crystals (EQCM measurements) and Pt disk (RRDE experiments). Electrodeposition efficiency, as estimated from EQCM experiments, was ca. 73 % and the thickness of the deposit was in the range of 1,500 atomic layers. A scanning electron microscope (LEO 435 VP) and EDX (Röntec EDR286) analysis showed that the obtained deposits tightly covered the substrate and no elements other than Co were detected; the latter was also confirmed by XPS analysis and will be discussed later.

The obtained Co deposits were examined in a standard three-electrode setup in 0.1 M KOH aqueous KOH (POCh, p.a.) solutions. Hg|HgO|0.1 M and Pt gauze wire or Au foil served as reference and counter electrodes, respectively. All potentials in the text are referred to Hg|HgO. All electrolyte solutions were prepared with Millipore water (18.2 MΩ cm). The electrolyte was deoxygenated by bubbling N_2 (99.999 %, Air Products) through the solution.

The electrochemical quartz crystal microbalance setup was composed of an EQCM crystal holder and controller (Model 230, Institute of Physical Chemistry, Warsaw, Poland), an EP20A potentiostat (Elpan), an EG20 (Elpan) linear sweep generator (Elpan), a Hewlett-Packard HP53131A universal counter and an Ambex LC-011-1612 ADC/DAC converter [34]. Gold-covered AT-cut 5 MHz quartz crystals (ITR, Poland) were used. EQCM was calibrated by means of Ag electrodeposition and stripping in 1.5 mM $AgNO_3$+0.1 M $HClO_4$.

The rotating ring disk electrode experiment was performed with an AFMT28T (Pine Instruments) Pt–Pt ring–disk electrode with collecting efficiency of 37 %, according to the manufacturer's data, and controlled by an AFMSRX modulated speed rotator (Pine Instruments) and a CHI 700C (CHInstruments) bipotentiostat. The electrochemical behaviour of Co layers with the thickness in the range of thousands of atomic layers was found to be generally the same for Pt and Au substrates used for electrodeposition [34].

Ultra-high vacuum XPS measurements were performed in the Institute of Physical Chemistry of Polish Academy of Sciences with an ESCALAB-210 (VG Scientific) apparatus using an Al X-ray gun. After completing the electrochemical experiments, the electrode was dried with N_2 stream, placed in a tightly closed glass vial filled with N_2 and transported to the XPS measurements facility.

The electrochemical impedance spectroscopy (EIS) measurements were applied to determine the double layer capacitance used for estimation of the real surface area of the electrodes. The experiments were carried out with a CHI660D potentiostat. AC signal in the frequency range 21,000–1 Hz with 5-mV amplitude was applied. The spectra acquisitions were preceded by 40 s of polarisation at

potentials of the measurements. The spectra were fitted with Equivcrt software [39].

Results and discussion

Real surface area determination

The double layer capacitance measurements, by means of EIS, were applied to determine the real surface area of the Co electrodes studied. Co(II) compounds, CoO and Co $(OH)_2$, possess semiconducting properties [40] and the interfacial capacitance measured at potentials of surface oxidation contains contributions from the double layer capacitance and from the capacitance of these compounds. A separate determination of the double layer capacitance and the capacitance of thin, semiconducting oxides/hydroxides is then required if the capacitance measurements are to be applied to estimate the real surface area. This, however, can be complicated. Further complications are related to the fact that CoO and $Co(OH)_2$ might differ in respect to semiconducting properties. As a result, the contribution from the capacitance of the oxidised layer might change with its composition. In such a case, tracking of the oxidation kinetics by the interfacial capacitance measurements is complicated. Hence, the capacitance was measured only in the potential range of hydrogen evolution (HER) where the Co surface is reduced (−1,300≥E≥−1,400 mV) without contribution from the capacitance of Co oxides/hydroxides. Examples of admittance spectra are shown in Fig. 1.

The spectra were fitted to the equivalent circuit presented in the top right inset in Fig. 1 [41, 42]. The double layer capacitance is expressed as a constant phase element (CPE) [43, 44] Eq. 1:

$$Z_{CPE} = Q^{-1}(i\omega)^{-\alpha} \tag{1}$$

where Q is the preexponential factor ($3.82\ 10^{-5}$–$4.42\ 10^{-5}$ $s^{\alpha}\Omega^{-1}cm^2$, apparently E independent), ω is angular frequency, i is the imaginary unit and α is an exponential parameter varying from 0 to 1 (the latter for pure capacitance). The obtained values of α were in the range of 0.91–0.92. The other components of the circuits include ohmic resistance, R_{ohm}, and the charge transfer resistance of HER, R_1. Z_{CPE} was recalculated into the capacitance according to Eq. 2 [44]:

$$C_{dl} = \left(Q\left({R_{ohm}}^{-1} + {R_1}^{-1}\right)^{(\alpha-1)}\right)^{1/a} \tag{2}$$

Because $R_{ohm} << R_1$, the C_{dl} values in Eq. 2 are determined by R_{ohm}.

The results of the fitting procedure are presented in Fig. 1 as solid lines, with the top left inset showing the calculated

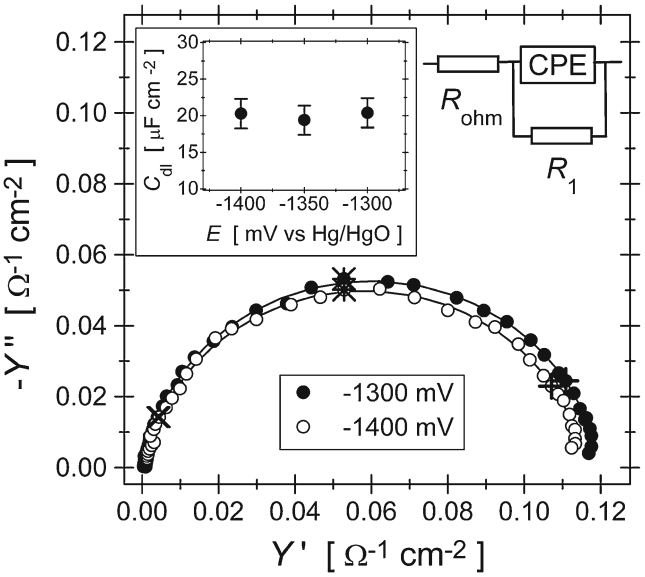

Fig. 1 Examples of impedance spectra recorded for an electrodeposited Co electrode in 0.1 M KOH at two potentials indicated on the plots and presented in admittance coordinates. *Points* experimental data, *lines* fit to the equivalent circuit presented in the *right top inset* (see details in the text). Points for 4,638.7 Hz (*plus sign*), 852.5 Hz (*asterisk*) and 97.7 Hz (*multiplication symbol*) are indicated. *Left top inset* calculated C_{dl} values as a function of potential

values of C_{dl} as a function of potential. For −1,300≥E≥−1,400 mV, the values of C_{dl} are practically potential independent. For this E range, we arbitrarily assume the specific double layer capacitance of 20 $\mu F\,cm^{-2}$, a typical value for aqueous electrolytes in the absence of significant specific adsorption [45]. The surface roughness factor obtained for the electrodes studied in this work was in the range of 19–33. The amount of the oxidised layer formed can be calculated on the basis of Co oxidation or Co(II) reduction charge. We assume that for solid cobalt with hcp structure and lattice constant of 0.251 nm [46], the charge required for complete oxidation of the topmost layer of Co atoms to Co (II) equals 587 $\mu C\,cm^{-2}$. In the further parts of the text, thickness is expressed in monolayers, which indicates the number of topmost layers of Co atoms completely oxidised, i.e. multiplicity of the charge of 587 $\mu C\,cm^{-2}$. In the case of Co(II) layer, the term monolayer means the amount of the oxidised layer containing the amount of Co(II) formed during complete oxidation of one full atomic layer of Co. When formation of a "chessboard-like" structure of the oxide/hydroxide is considered [2–4], such a Co(II) monolayer contains at least two atomic layers composed with mixed Co^{2+} and O^{2-} or OH^-, depending on the structure.

Cyclic voltammetry, EQCM and RRDE measurements

Figure 2 presents the cyclic voltammetry (bottom) and gravimetric (top) curves for an electrodeposited Co electrode

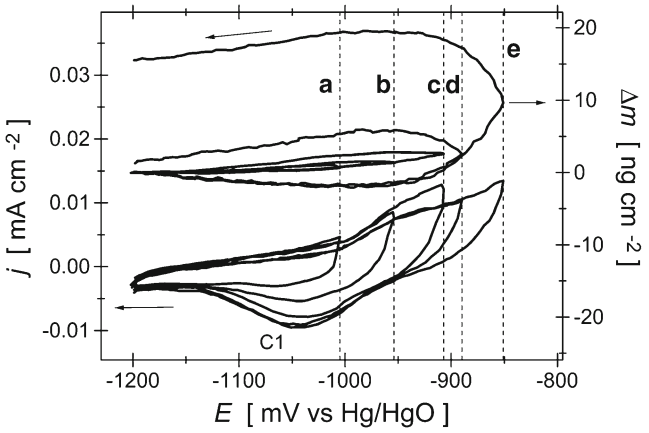

Fig. 2 Cyclic voltammetry (*bottom*) and gravimetric (*top*) curves for a Co electrode in 0.1 M KOH for various anodic potential limits indicated by *vertical lines*: *a* −1,005 mV, *b* −954 mV, *c* −907 mV, *d* −890 mV, *e* −810 mV. The order of changes of anodic potential limit was as follows: −1,005, −954, −907, −810 and −890 mV; 25 mV s^{-1}, room temperature; *C1* reduction peak (discussed in the text). The zero mass for gravimetric curves is arbitrarily set at −1,200 mV for all curves

in 0.1 M KOH_{aq} recorded from −1,200 mV to various anodic potential limits, E_a, below −851 mV. Co oxidation currents start at potentials more negative than hydrogen evolution onset (located at ca. −932 mV) and rise with the potential increase. These currents are accompanied by an increase in the mass of the electrode, also observed at potentials more negative than HER onset. The cathodic branch of CV curves exhibits a peak, C1, at ca. − 1,040 mV, which is accompanied by a mass decrease due to reduction of Co(II) compounds. Peak C1 partially overlaps HER currents. For $E_a \geq -890$ mV, the mass loss due to surface reduction extends below the apparent end of C1 peak and the mass loss is also observed during the initial stages of the subsequent anodic cycle (up to ca. −1,040 mV). This indicates that Co(II) layer reduction extends beyond the C1 peak towards the region of HER.

In [34], it was shown that continuous potential cycling of a Co electrode with anodic potential limit of −700 mV results in the formation of a hardly reducible layer of Co (II) compounds. In Fig. 2, the irreversibility of the oxidation process is mirrored by an evolution of CV and EQCM curves. Oxidation currents recorded for $E_a = -890$ mV and after previous scans to $E_a = -851$ mV are smaller than the currents recorded before E_a was increased to −851 mV ($E_a = -954$ and −907 mV in Fig. 2). For $E_a \leq -907$ mV, the gravimetric curve is closed, indicating the insignificance of irreversible oxidation and dissolution. When E_a increases beyond −907 mV, the gravimetric curve becomes open due to the accumulation of a hardly reducible oxidised layer [34]. Further increase in E_a results in continuous evolution of both gravimetric and cyclic voltammetry curves, until a closed gravimetric loop is obtained, similarly to the results obtained in 1 M KOH [34] (results not shown).

Figure 3 shows the ring currents recorded in RRDE experiments in 0.1 M and 3 M KOH at 2,500 r.p.m. for two ring potentials (E_r): −1,150 mV, where Co^{2+} species are reduced, and 0 mV, where Co^{2+} are oxidised to Co^{3+}. The potentials were not corrected for liquid junction potential between 0.1 M (reference electrode) and 3 M (working electrolyte) KOH. Considering the estimated mobility of K^+ ions [47], such a potential difference should not exceed 30 mV [48], which is not a significant figure as compared to the potential span of applied E_r values.

When the disk potential (E_d) is scanned at potentials more positive than −950 mV, we observe an increase in currents recorded in 3 M KOH, cathodic currents for $E_r = -1{,}150$ mV and anodic ones for $E_r = 0$ mV, due to the reduction and oxidation of Co(II) soluble species, respectively (Fig. 3). These effects are absent in 0.1 M KOH, indicating the insignificance of Co dissolution in the latter medium. Other features observed on ring currents are attributed to processes of hydrogen evolution and oxidation. Hence, a decrease in cathodic current observed for both concentrations when E_d is scanned in the positive direction from −1,250 to −1,100 mV can be explained as a result of the influence of disk reactions on hydrogen evolution on Pt ring. The decrease in the anodic ring current observed in 0.1 M KOH for $E_r = 0$ mV and for E_d changes from −1,250 to −1,100 mV and which is absent in 3 M KOH is related to the oxidation of H_2 generated during cathodic polarisation. Because the solubility of H_2 decreases with the increase in KOH concentration [49], this effect is less important for a higher concentration of KOH. Based on RRDE results, we can conclude that the solubility of electrodeposited Co electrode polarised up to −800 mV in 0.1 M KOH is negligible and that the dissolution process cannot be considered as a step in the formation of the oxidised layer.

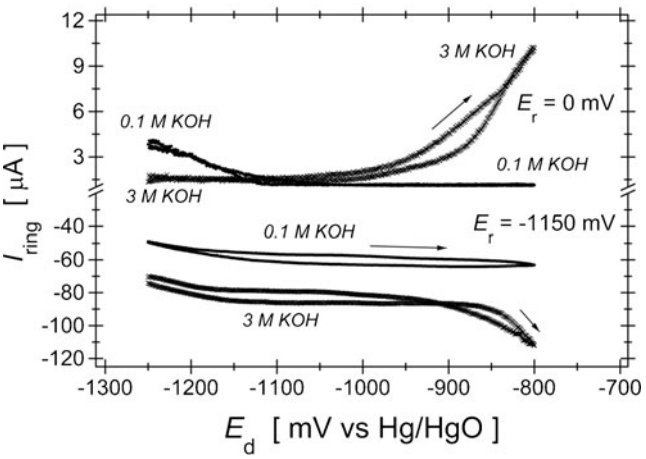

Fig. 3 Ring currents vs. disk potential for RRDE with the ring polarised at −1,250 and 0 mV at 0.1 and 3 M KOH, 2,500 r.p.m. Disk potential scanned with 50 mV s^{-1} from −1,250 to −800 mV. The *arrows* indicate the direction of changes in disk potential

Constant potential oxidation

The kinetics of Co oxidation at a constant potential value was studied by means of cyclic voltammetry, chronoamperometry, and EQCM. The irreversibility of the surface oxidation process was tested in separate EQCM experiments composed of three steps: (a) prereduction at −1,200 mV, (b) oxidation at a specified potential for a specified time and (c) reduction at −1,200 mV of the oxidised layer formed in step b. The degree of removal of the oxidised layer during reduction, Δm_{irrev}, is defined as the difference between the mass measured at −1,200 mV in step a, i.e. before the oxidation, and the mass measured in step c, for the reduction time for which the mass becomes approximately constant. This parameter mirrors the reversibility of the oxidation process and is presented in Fig. 4 for various E_{ox}. For E_{ox} of −950 mV, the oxidised layer is fully reduced, even for t_{ox} up to 178 s. For higher E_{ox} values, Δm_{irrev} increases with an increase in E_{ox} and t_{ox}, indicating the dependence of the oxidation reversibility on E_{ox} and on the amount of the oxidised layer formed. A similar result is obtained when the reduction potential in steps a and c is shifted to more negative values down to −1,350 mV. Due to the irreversibility of the oxidation process, the E_{ox} and t_{ox} values were limited to −880 mV and ca. 64 s, respectively.

Figure 5 presents examples of the influence of oxidation time ($2 \le t_{ox} \le 45$ s.) at −940 mV on the shape of the cathodic branch of the cyclic voltammetry curves. An increase in t_{ox} leads to an increase of the charge of peak C1. An increase in t_{ox} also leads to an increase in reduction currents at potential more negative than the apparent end of peak C1 ($E<-1{,}200$ mV; Fig. 5). For higher t_{ox} values, an inflection at ca. −1,200 mV is observed, suggesting the formation of an additional reduction peak at $E<-1{,}200$ mV. It is likely that Co(II) reduction may not be completed in the potential range of the C1 peak. This is in line with EQCM results (Fig. 2) showing that for higher values of E_a the mass loss due to Co(II) reduction is observed also after the apparent end of peak C1.

For charge calculation purposes, currents not related to Co(II) reduction, i.e. due to HER and the double layer charging, were eliminated by subtraction of the currents obtained for the shortest t_{ox} applied, 2 s, from the currents obtained for $t_{ox}>2$ s. The integration covered the potential range from the beginning of peak C1 to the potential where the currents for $t_{ox}=2$ s and $t_{ox}>2$ s overlap. The left inset in Fig. 5 presents semi-logarithmic plots of t_{ox} influence on such calculated reduction charges, q_{red}, which were obtained for various E_{ox} values. The plots can be approximated by straight lines, indicating the applicability of the direct logarithmic law of the surface oxidation. Interestingly, good linearity is observed also for $E_{ox}>-920$ mV for which only a fraction of the oxidised layer is reduced (Fig. 4). A linear relation between the charge and $\ln(t_{ox})$ is observed also for q_{red} obtained by integration in potential range of peak C1 only (results not shown). For $E_{ox} \le -980$ mV, the values of

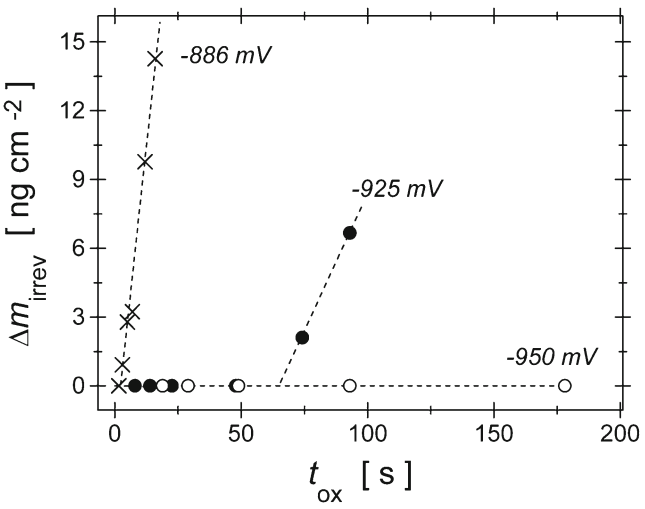

Fig. 4 Oxidation potential and time influence on reversibility of the oxidation process expressed as a mass difference, Δm_{irrev}, measured at −1,200 mV before the oxidation and at −1,200 mV after reduction of the oxidised layer formed at specified potential for a specified time. The reduction −1,200 mV was continued until a nearly constant mass was established. *Lines* are meant as a guide to the eyes

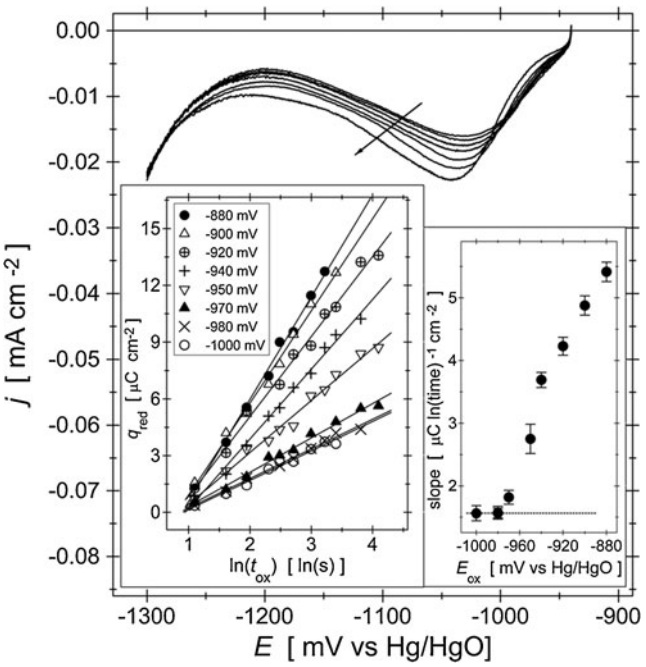

Fig. 5 *Top* examples of cathodic sections of cyclic voltammetry curves (100 $mV s^{-1}$) for a Co electrode in 0.1 M KOH and oxidised at −940 mV for various oxidation times: 2, 3, 5, 7, 12, 20 and 45 s. The *arrow* indicates changes in the curve resulting from an increase in polarisation time. *Left inset* influence of the oxidation time, t_{ox}, on the charge of Co(II) reduction, q_{red}, presented in semi-logarithmic coordinates; oxidation potentials are indicated on the plot. *Right inset* slope of q_{red} vs. $\ln(t_{ox})$ plots from the right inset vs. oxidation potential. The *horizontal line* indicates the region with the slope independent on E_{ox}

the slope of these lines are independent on E_{ox}, while for higher oxidation potentials the slope increases with E_{ox} (right inset in Fig. 5). It should be pointed out that for E_{ox}>−920 mV, the measured values of the slopes are most likely reduced due to the incomplete reduction of the oxidised layer (Fig. 4), but their increase with E_{ox} indicates an increase in the oxidation rate with increasing potential also for this E_{ox} range.

Figure 6 presents mass change, Δm, vs. oxidation charge, q_{ox}, profiles for constant potential oxidation for E_{ox} changing from −1,000 to −890 mV. Before applying E_{ox}, the electrode was reduced at −1,250 mV. Qualitatively and quantitatively similar results are obtained also for prereduction at −1,350 mV. q_{ox} was obtained by integration of chronoamperometric curves. For potentials in the HER region (E_{ox}<−926 mV), the charge due to Co oxidation used for construction of the plots was taken only for a short period of t_{ox} when the oxidation current is much higher than the steady state currents due to HER. Hence, for E_{ox}<−926 mV, the plots cover only a very narrow range of q_{ox} values. We note that when extrapolated steady state HER currents are subtracted from Co oxidation currents the obtained values of the slopes of mass vs. charge plots change by no more than ca. 7 % as compared to that presented in Fig. 6. One notes that for E_{ox}<−916 mV the plots can be approximated by single straight lines over the whole t_{ox} period. Such a constant mass-to-charge ratio indicates that the composition of the oxidation products does not change with the progress in the process. For E_{ox}≥−916 mV and q_{ox}>0.05 mC cm^{-2}, a departure from linearity is observed and an additional one linear section is established. This effect takes place in the E_{ox} range where an increase in the irreversibility of the oxidation process, i.e. $\Delta m_{irrev}\neq 0$, is observed (see Fig. 4).

The slopes of Δm vs. q_{ox} plots can be recalculated into mass per mole ratios, M_a. The latter value represents the mass change per number of the electrons exchanged in the process and is shown in the inset in Fig. 6a as a function of E_{ox}. For E_{ox}≥−916 mV, the inset displays M_a values only for the initial linear section of Δm vs. q_{ox} plots for low values of t_{ox}. Comparative experiments performed in 0.1 M $NaOH_{aq}$ show no influence of cation identity: M_a obtained for NaOH were within±6 % of the values for 0.1 M KOH. The maximum value of M_a of ca. 12.5 gmol^{-1} is obtained for E_{ox}=−988 mV. For the lowest E_{ox} applied (−1,000 mV), the M_a value is ca. 11.3 gmol^{-1}. An increase in potential above −988 mV leads to a decrease in M_a, which eventually reaches the value in the range of 6.5–5.5 gmol^{-1} for E_{ox}>−922 mV.

The presented M_a values point to changes in composition of the Co oxidation products: the oxidised layer formed at E_{ox}<−970 mV contains significant amounts of $Co(OH)_2$ (theoretical M_a=17 gmol^{-1}), while at more positive potentials the presence of CoO is detected (theoretical M_a=8 g mol^{-1}). These conclusions are in line with XPS results which are discussed further in the text. The obtained order

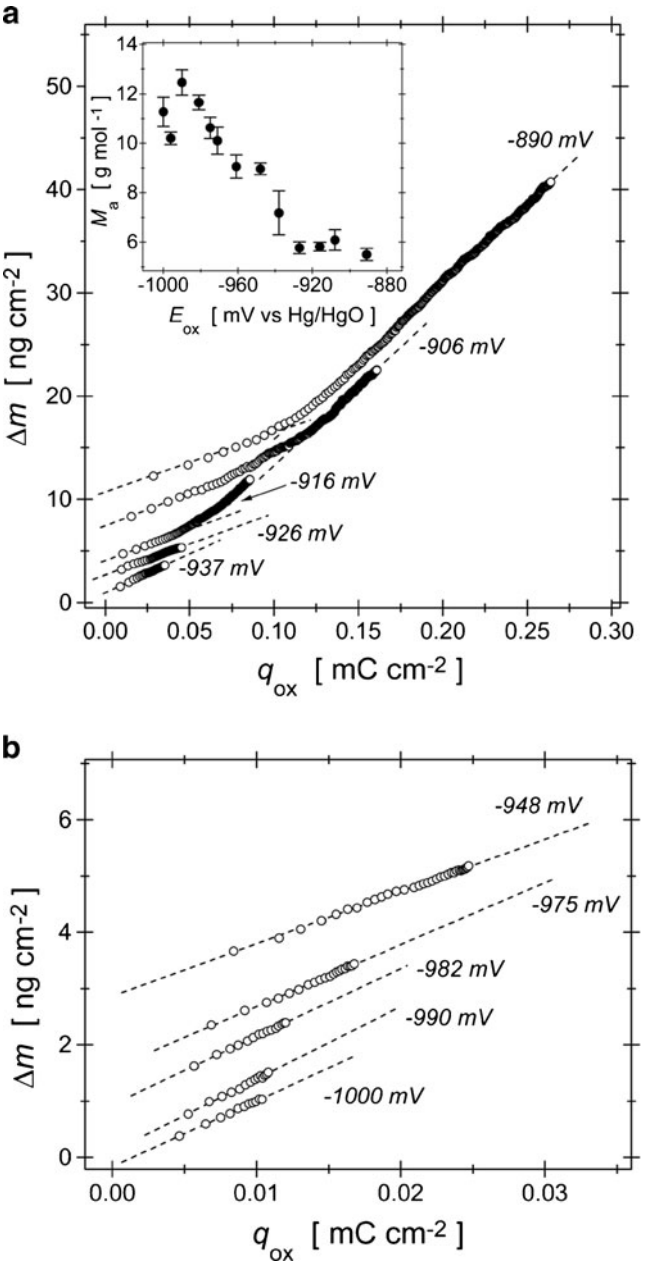

Fig. 6 Mass change, Δm, vs. oxidation charge, q_{ox}, profiles recorded during oxidation of a Co electrode in 0.1 M KOH at various E_{ox}: **a** from −937 to −890 mV, **b** from −1,000 to −948 mV. For clarity, the *curves* for various values of E_{ox} are arbitrarily shifted in the mass scale. Application of the oxidation potential was preceded by a reduction of the electrode at −1,250 mV. *Inset* in **a**, influence of the oxidation potential on molar mass of Co oxidation products, M_a, obtained from the slopes of Δm vs. q_{ox} plots

of formation of Co(II) compounds corresponds well to the order of standard potentials, E^0, of $Co(OH)_2$ and CoO [22, 50, 51], with E^0 of the latter being more positive than for $Co(OH)_2$. The fact that the obtained M_a values are smaller than the ones theoretically predicted is attributed to participation of adsorbed H_2O/OH^- in the oxidation process. For E_{ox}<−970 mV, the lowering of M_a values due to a contribution

from the formation of some amounts of CoO should also be considered. A comparison of Figs. 4 and 6 indicates the existence of a relation between the oxidised layer composition and the reversibility of the oxidation: $\Delta m_{irrev} \neq 0$ is observed for E_{ox} range where M_a falls below 8 $g mol^{-1}$ (Fig. 4).

Intermediate values of M_a observed in the inset in Fig. 6a for $-975 \leq E_{ox} \leq -930$ mV point to generation of a layer composed of both CoO and $Co(OH)_2$. The formation of a layered structure composed of the oxide and hydroxide was proposed for Co oxidation in alkaline electrolytes on the basis of ellipsometric measurements [52]. This was observed, however, for the multilayered oxidised layers with thickness in the range of a few nanometers. The thickness of the oxidised layers studied in this work can be estimated on the basis of the oxidation charges. For $E_{ox}=-890$ mV and $t_{ox}=64$ s, we obtain the surface coverage of ca. 45 %. This value suggests that for $-975 \leq E_{ox} \leq -930$ mV, the CoO and $Co(OH)_2$ should form separate 2D areas rather than a multilayered 3D structure.

The second linear section of Δm vs. q_{ox} plots observed for E_{ox} −916 mV and for longer t_{ox} values has a slope of ca. 15 $g mol^{-1}$. We attribute this value to the formation of hydrated CoO rather than $Co(OH)_2$, the effect being confirmed by XPS results which are presented in the later part of the text, showing the formation of significant amounts of CoO in this E_{ox} range. As it will be shown later, Co(II) layer compositions determined from EQCM measurements correspond to XPS results (Fig. 9), indicating that EQCM response can be interpreted in terms of pure mass changes.

When the molar mass of the oxidation products does not change during the process, the Δm vs. t_{ox} profiles are indicators of the kinetics of the reaction with similar mathematics applied as in the case of charge vs. time relation. Figure 7 shows Δm vs. $\ln(t_{ox})$ plots for Co oxidation at $-1{,}000 \leq E_{ox} \leq -890$ mV and for t_{ox} of up to 8.6–64 s. The respective q_{ox} vs. $\ln(t_{ox})$ plots are presented in Fig. 8; for $E_{ox} < -916$ mV, the charge used for construction of the plots is the one recorded for the initial t_{ox} period when the oxidation current is much higher than the steady state HER currents. Both figures were constructed on the basis of the data presented in Fig. 6.

The inset in Fig. 8a shows a magnification of initial sections of chronoamperometric curves recorded with RRDE at two oxidation potentials and for two rotation rates. The shape of these transients is typical for all E_{ox} values applied and also for stationary constant potential oxidation. One would note the absence of a nucleation peak [53, 54], indicating that the nucleation and growth models, both 2D and 3D with bulk and surface diffusion, are not applicable. Rotation rate-independent current transients indicate that the rate of the oxidation process is not determined by transport in the electrolyte.

Figures 7 and 8 show that:

1. For $E_{ox} < -948$ mV, the Δm vs. $\ln(t_{ox})$ plots reveal a good linearity for the entire t_{ox} range (Fig. 7). For higher E_{ox} values, only the initial section of the plots is linear; for longer t_{ox} values, a departure from linearity is observed: downwards for $E_{ox}=-937$ and −948 mV and, more pronounced, upwards for $E_{ox} \geq -926$ mV.

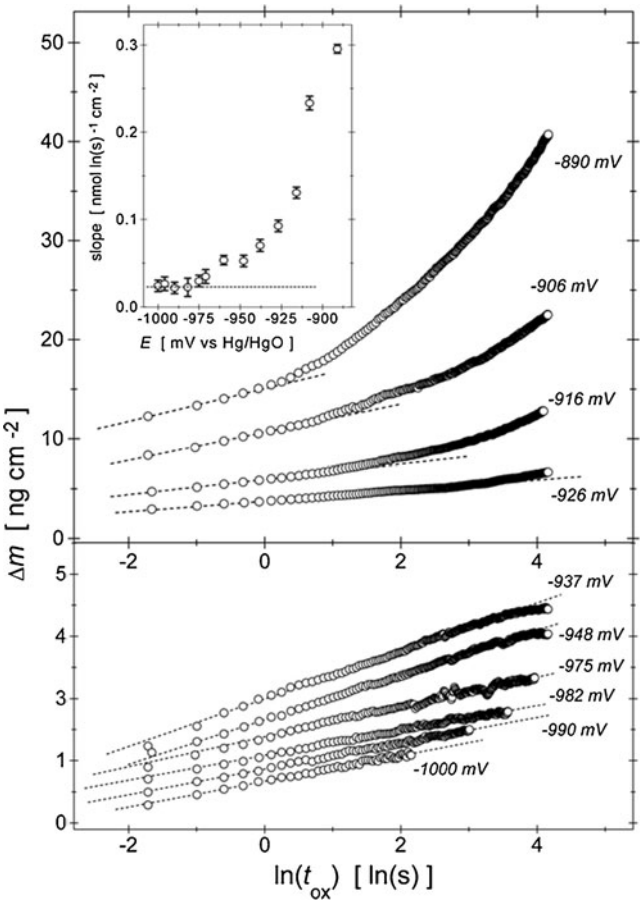

Fig. 7 Semi-logarithmic plots of mass change, Δm, vs. oxidation time for oxidation of a Co electrode in 0.1 M KOH for various oxidation potentials indicated on the plot (data from Fig. 6). For clarity, the curves for various values of E_{ox} are arbitrarily shifted in the vertical scale. The *inset* shows slopes of Δm vs. $\ln(t_{ox})$ plots as a function E_{ox}. The *horizontal line* in the inset indicates the region where the slope is independent on E_{ox}. The *error bars* for the inset are comparable to the size of the points

2. For $E_{ox} < -916$ mV, the q_{ox} vs. $\ln(t_{ox})$ plots are linear with a single slope over the whole t_{ox} range presented (Fig. 8). It should be noted that the oxidation currents recorded in this E_{ox} range can be influenced by contribution from parallel currents due to HER. However, the good linearity of q_{ox} vs. $\ln(t_{ox})$ plots correspond well to the linear shapes of Δm vs. $\ln(t_{ox})$ (Fig. 7) and q_{red} vs. $\ln(t_{ox})$ (Fig. 5) plots observed in the same range of E_{ox}. This indicates that the plots presented in Fig. 8 can be treated as reliable indicators of Co oxidation mechanism even at potentials of HER. For $E_{ox} \geq -916$ mV, two linear sections are observed in Fig. 8. The length of the first linear section (low t_{ox} values) decreases with an increase in E_{ox}. The second linear section, observed for $E_{ox} \geq -916$ mV, has a higher slope, starts at

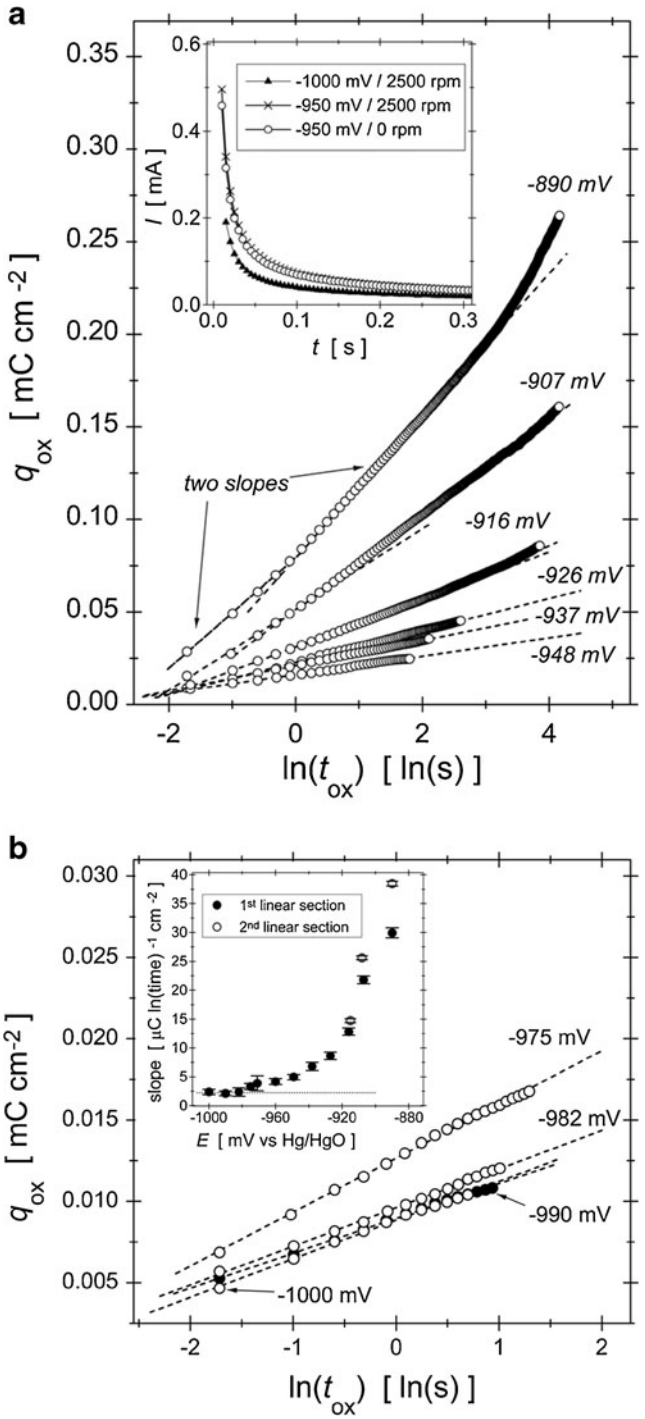

Fig. 8 Semi-logarithmic plots of oxidation charge, q_{ox}, vs. oxidation time recorded during constant potential oxidation in 0.1 M KOH at various E_{ox} (data from Fig. 6): **a** from −948 to −890 mV, **b** from −1,000 to −975 mV. The *arrows* in **a** indicate the two slopes of the linear section of the plots discussed in the text. *Inset* in **a**, initial sections of chronoamperometric curves for oxidation of a Co electrode in RRDE experiments for two oxidation potentials: −1,000 mV (2,500 r.p.m.) and −950 mV (disk currents, 2,500 and 0 r.p.m.). *Inset* in **b**, slopes of q_{ox} vs. $\ln(t_{ox})$ plots as a function E_{ox}. The *horizontal line* in the inset indicates the region where the slope is independent on E_{ox}. The *open circles* represent the slopes of the second linear sections observed for E_{ox}>−920 mV and discussed in the text. The *error bars* for the inset are comparable to the size of the points

longer oxidation times and extends to $\ln(t_{ox})$ of ca. 3.2, where further changes in the shape of the plots are seen.

3. The slopes of linear sections of both Δm vs. $\ln(t_{ox})$ and q_{ox} vs. $\ln(t_{ox})$ plots are presented in insets in Figs. 7 and 8b, respectively. For Δm vs. $\ln(t_{ox})$ plots, the slopes were divided by M_a/F, where F is the Faraday constant. Such obtained values are independent on the composition of the oxidation products and are direct indicators of the kinetics of the process for t_{ox} range for which M_a is constant (Fig. 6). One notes that for $E_{ox} \leq -980$ mV, the slopes are independent on E_{ox} (insets in Figs. 7 and 8b, respectively). For $E_{ox} > -980$ mV, the slopes of both plots increase with an increase in E_{ox}. A similar shape of slope vs. E_{ox} relation was obtained also from cyclic voltammetry measurements (Fig. 5).

4. The values of the slopes obtained from CV (Fig. 5) are smaller compared to CA (Fig. 8b): from 1.5 to 1.9 times for E_{ox} below −920 mV and up to 5.8 times for −880 mV. These differences mirror the complications with separation of overlapping currents of HER and Co(II) reduction in CV experiments. Further on, the irreversibility of Co(II) formation for $E_{ox} > -920$ mV leads to an incomplete reduction of Co(II) layer during single, negative CV scan and increases the differences between values of the slopes obtained for CV and CA.

5. Changes in the shape/slope of Δm vs. $\ln(t_{ox})$ and q_{ox} vs. $\ln(t_{ox})$ plots (Figs. 7 and 8) can be linked to the evolution of Δm vs. q_{ox} curves (Fig. 6). Δm vs. q_{ox} plots exhibit departures from linearity for $E_{ox} \geq -926$ mV and this corresponds to (a) a departure from linearity of Δm vs. $\ln(t_{ox})$ plots ($E_{ox} \geq -926$ mV in Fig. 7) and (b) the appearance of the second linear section in q_{ox} vs. $\ln(t_{ox})$ curves ($E_{ox} \geq -916$ mV in Fig. 8a).

X-ray photoelectron spectroscopy

Very thin oxidised layers with estimated thickness not greater than 50 % of the monolayer are hard to measure using ex situ techniques. Complications are related to the disputable stability of such thin layers when examined under ex situ conditions and to the accuracy of separation of a small Co(II) photopeak from a prevailing Co(0) signal. In order to obtain more reliable results of ex situ measurements, the XPS technique was applied for the analysis of the oxidised layers with thickness greater than those presented in Figs. 6, 8 and 9.

Figure 9 presents the XPS spectra recorded for Co samples oxidised for 300 s at two potentials (−980 (Fig. 9b) and −890 mV (Fig. 9c)) and for a Co deposit subjected to etching with Ar^+ gun (Fig. 9a). A detailed discussion of the structure of Co(II) spectra can be found elsewhere [55–58]; here we focus mainly on the binding energies of main, non-deconvoluted Co 2p3/2 peak and its satellites located at higher energies. For Ar-sputtered Co(0) (Fig. 9a), we observe the main 2p3/2 peak at 778.2 eV and a 2p1/2 peak at 793.2 eV, in agreement with the literature [55, 59]. The

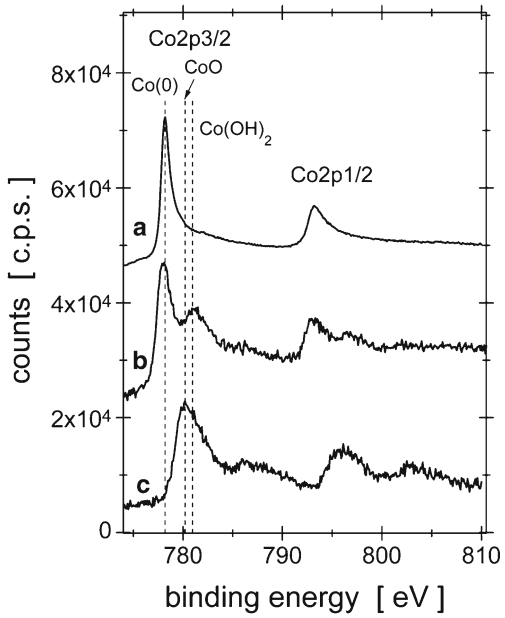

Fig. 9 XPS spectra recorded for Co electrodes studied (*a*) after cleaning by Ar^+ sputtering and after oxidation (*b*) at −980 mV for 300 s and (*c*) at −890 mV for 300 s. The *vertical lines* show the locations of 2p3/2 peaks for Co(0) (778.2 eV), Co(II) in CoO (780.2 eV) and Co(II) in $Co(OH)_2$ (780.9 eV)

satellite of 2p3/2 peak is usually poorly developed (ca. 781 eV [55]) and cannot be distinguished from spectrum a without deconvolution. Figure 9a indicates that the obtained electrodeposits are composed of the metallic Co. The spectrum for −980 mV (Fig. 9b) shows a decrease in Co(0) peaks upon oxidation time and reveals new developing peaks: broad 2p3/2 peak at ca. 780.9 eV and 2p1/2 at 796.5 eV. The spectrum recorded for the sample oxidised at −890 mV shows Co(II) peaks at energies lower than for −980 mV: a main 2p3/2 peak at 780.2 eV with a satellite at 785.7 eV and a 2p1/2peak at 796.2 eV with a satellite at 803 eV.

Literature data [55, 58, 59] indicate that for CoO the 2p3/2 and 2p1/2 peaks are located at binding energies lower than for $Co(OH)_2$. The spectra shown in Fig. 9 indicate the existence of $Co(OH)_2$ at −980 mV and CoO at −890 mV, in agreement with EQCM data (Fig. 6). The fact that the XPS results are in line with EQCM data indicates that the frequency response of the microbalance is determined by pure mass changes. We note that for E_{ox}=−890 mV (Fig. 9 (c)), the ratio between areas of 2p1/2 peak and its satellite is ca. 2, indicating the absence of Co(III) forms for which the satellite should be much smaller as compared to the main 2p1/2 peak or even not observed [55, 60].

Discussion of the oxidation model

Three independent techniques, CV, CA and EQCM, reveal that early stages of Co oxidation in an alkaline electrolyte, i.e. up to ca. 50 % of the single monolayer, follow a direct logarithmic law (Figs. 5, 7 and 8). These three techniques also reveal that for E_{ox}>−980 mV, the slope of semi-logarithmic plots increases with E_{ox}, while for lower oxidation potential values the slope is E_{ox} independent (insets in Figs. 5, 7 and 8b).

For electrochemical oxidation, the direct logarithmic law of oxide/hydroxide growth was discussed in [4, 6, 8] and the respective models have been derived. In [4], it was assumed that oxidation leads to the formation of a chessboard-like structure with uniformly mixed metal and oxygen/OH^- ions. The rate-determining step (r.d.s.) in this model is a rotation of metal–oxygen dipoles in the electric field established at the interface ("place exchange" model). The main equation used in this model has the following form (one electron transfer [1, 4]) Eq. 3:

$$q = a\ln(t_{ox}) + b \tag{3}$$

with Eq. 3a:

$$a = \frac{d_{ML}A_r RTF\varepsilon_0}{2N_A^2\beta\mu^2} \tag{3a}$$

where β is the symmetry factor (assumed to be 0.5), μ is the dipole moment of rotating species, d_{ML} is the thickness of the monolayer of rotating species and the other parameters have their usual meaning. The intercept b is a function of A_r, μ, β and ε_0 and depends also on a rate constant, k, potential drop across the layer of the dipoles, ΔE, and on the surface potential due to the presence of water molecules in the double layer, $\Delta\varphi$. The exact mathematical form of the intercept is presented in [1, 4], and in this paper we do not discuss this parameter in detail since it contains too many unknown parameters (k, ΔE, $\Delta\varphi$). The dependence of the intercept b on potential is complex [1, 4], while the slope of Eq. 3 is potential independent. This model was applied mainly for the formation of oxidised layers with thickness not greater than that of the monolayer [1–3], which corresponds to the range of thickness of Co(II) layers studied in this work.

The model considered in [6] assumes the oxidation process following nucleation and growth pathway. The following equation was derived [6] Eq. 4:

$$q = a'\eta\log(t_{ox}) - \frac{a'\eta}{6}\log(q) + b' \tag{4}$$

with Eq. 4a:

$$a' = \frac{3ze_0}{\Pi v f k_B T\sigma^2} \tag{4a}$$

where v is the volume of the molecule, z is the number of the electrons exchanged, e_0 is the elementary charge, η is the

overpotential, σ is the surface free energy, f is a factor used for conversion between charge and thickness units and the other terms have their usual meaning. Similarly to Eq. 3, the intercept b' in Eq. 4 is a function of a' and depends also on η and on the electrochemical rate constant [6]. When $a'\eta$ is not greater than unity, the term containing $\log(q)$ can be neglected in Eq. 4 and the slope of the semi-logarithmic relation between the charge and $\log(t_{ox})$ is a linear function of the potential.

The point defect model [8, 61, 62] also predicts a linear relation between the amount of the oxidised layer formed and $\ln(t_{ox})$ with the slope inversely dependent on the electric field, i.e. applied potential. This model, however, is predicted for the thickness above one monolayer [8], beyond the thickness range studied in the present work.

The existence of a potential-independent slope of semi-logarithmic plots, in agreement with the "place exchange" model Eq. 3, is observed in Figs. 5, 7 and 8b for $E_{ox} \leq -980$ mV. This E_{ox} range corresponds well to potentials where $Co(OH)_2$ is the prevailing product of the oxidation process (Fig. 6a). Application of the "direct logarithmic law" model for the formation of $Co(OH)_2$ requires some assumptions about the details of the process. First, we assume that both electrons to be exchanged during Co atom oxidation are transferred in separate steps [63–65]. The first step in the oxidation process would then be the formation of Co(OH) structures at the electrode surface. Further on, it is likely that the rotating species is Co(OH) rather than $Co(OH)_2$ since the former should possess a relatively high dipole moment. Hence, the order of the steps in the process of Co oxidation at $E_{ox} \leq -980$ mV is expected to be the same as for Ni oxidation as discussed in [7]: (1) fast transfer of the first electron to form Co(OH), (2) slow rotation of Co(OH) dipole (rate-determining step) and (3) fast transfer of the second electron and formation of Co(II) hydroxide molecule.

At $E_{ox} > -980$ mV, where the presence of CoO is detected (Figs. 6 and 9), the values of the slopes in Figs. 5, 7 and 8b are higher than for $Co(OH)_2$ region and, in contrast to Eq. 3, the slopes strongly depend on E_{ox}. As was discussed earlier (Fig. 6a), for $-975 \leq E_{ox} \leq -930$ mV, the electrode surface contains oxidised areas composed of CoO and $Co(OH)_2$. We assume that the formation of CoO and $Co(OH)_2$ proceeds independently, both according to the direct logarithmic law. Increasing the contribution from CoO would result in continuous changes of the slopes with E_{ox}. However, due to a contribution from OH bond, the Co(OH) dipole moment should be smaller than for CoO and slope a in Eq. 3a in the potential region of CoO formation should be smaller than for $Co(OH)_2$, opposite to what is seen Figs. 5, 7 and 8b. Further on, the slope of the first linear section from Fig. 8a increases also at potentials where the oxidised layer composition is unchanged (constant M_a in Fig. 6a). Thus, it is likely that the rate of oxidation not only depends on the composition but is also strongly influenced by the oxidation potential itself. The nucleation model (Eqs. 4 and 4a) also seems to be not applicable. The current–time profiles recorded for Co oxidation (inset in Fig. 8a) do not exhibit a nucleation peak, usually observed for nucleation and growth mechanism. Although a model of 2D layer growth controlled by instantaneous nucleation and according to Avrami theorem predicts a current decay without the peak [66], a linear relationship between the charge and $\ln(t_{ox})$ is not obtained [66]. Further on, Eq. 4 predicts a linear relation between the slope of q vs. $\ln(t_{ox})$ plots and potential, while Figs. 5, 7 and 8b indicate that the relation can be roughly approximated by a straight line only for CA.

A potential influence on the slope of the direct logarithmic law describing metal oxidation (Eqs. 3 and 3a) was observed for oxidation of Au [4] and Pt [5] in acidic solutions and for polycrystalline Ni in 0.5 M KOH [7]. In the case of Au, the effect was explained as a result of anion adsorption, while for the nickel it was attributed to various oxidation rates of different crystallographic planes exposed to the electrolyte. In all of these cases, however, the potential influence on the slopes was smaller than those presented in Figs. 5, 7 and 8b (ca. 270 % for 200 mV range for Au [4], ca. 100 % for 200 mV range for Pt [5] and below 10 % for 200 mV range for Ni (room temperature [7])) as compared to 300–900 % for 100 mV range measured in this work for CV and CA, respectively. Such huge changes cannot be attributed to the influence of crystallographic orientation on the oxidation process, especially when one considers that the potential influence on the slope of the direct logarithmic law was observed also for Pt single crystals [5]. Intuitively, the extent of the potential impact of the discussed slopes cannot be attributed to the contribution from E-dependent ion adsorption. When adsorption of cations is excluded (discussion of Fig. 6), the only ion which can adsorb on the electrode surface is OH^-. These ions do not block the surface for surface oxidation and most likely participate directly in the surface oxidation process. They may affect the surface oxidation process by changing the electric field at the interface, but the extent of this effect seems to be rather smaller than the E_{ox} influence on the slopes of the plots in Figs. 5, 7 and 8b.

The discussed potential influence on the slopes of semi-logarithmic plots cannot be also attributed to the irreversibility of the oxidation process: the effect of the slope increase is observed already for E_{ox} and t_{ox} range where the oxidation process can be considered as reversible (Fig. 4).

The preceding discussion shows that oxidation of Co in 0.1 M KOH at $E_{ox} > -980$ mV cannot be successfully described by already known oxidation models [4, 6]; a new model of surface oxidation process should be considered.

The presented results allow us to draw some conclusions which may be helpful in the development of a new surface oxidation model. The most striking difference between processes taking place above and below −975 mV is related to the form of oxygen containing species present in the oxidised layer. For $E_{ox}<-975$ mV, this is mainly OH^-, while for $E_{ox}>-975$ mV the oxidised layer contains significant amounts of O^{2-}. While OH^- ions are present in the electrolyte or can be easily formed during H_2O dissociation, O^{2-} must be generated in a separate reaction of H_2O/OH^- decomposition and such a step must be included in the overall oxidation mechanism for $E_{ox}>-980$ mV. Further on, the direct logarithmic law requires the driving force of the process to decrease with the progress in the process (or, alternatively, energy barrier must increase with the progress). Next, a smooth transition between mechanisms taking place below and above −980 mV is expected when E_{ox} increases. Finally, it is likely that the r.d.s. is not the electron transfer, which is assumed to be very fast, but other process, e.g. H_2O decomposition to form O^{2-} or phase oxide formation.

Based on the cited suppositions, we can briefly discuss the possible steps contributing to Co oxidation process at $E_{ox}>-980$ mV. When E_{ox} increases, the rate of transfer of both electrons also increases, and for high-enough values of E_{ox} the transfer of the second electron may proceed before the slow "place exchange" step [4]. This leads to the formation of Co^{2+} species stabilised at the surface by interaction with OH^- or H_2O. In the subsequent steps, OH^-/H_2O decompose to generate O^{2-}, and a phase oxide is formed. The latter steps are expected to be the r.d.s. (fast transfers of both electrons are treated as in a pseudo-equilibrium state). Charged species take part in H_2O decomposition to O^{2-}, and the rate of this step may depend on E_{ox}. The electric field at the interface changes with oxidation progress due to the formation of oxide, and this may increase the energy barrier when t_{ox} increases, leading to the shape of time profiles shown in Figs. 5, 7 and 8. The said scenario resembles an EEC mechanism but with the rate of the chemical step (C) affected by the electric field at the interface.

Conclusions

The oxidation of electrodeposited cobalt electrodes has been studied in 0.1 M KOH_{aq} solution in the potential range −1,000 to −880 mV vs. Hg|HgO where Co(II) compounds are formed. Four electrochemical techniques were applied to study the mechanism of the process: cyclic voltammetry, chronoamperometry, electrochemical quartz crystal microbalance and rotating ring disk electrode. We found that:

- The solubility of electrodeposited Co in 0.1 M KOH at potentials more negative than −800 mV vs. Hg|HgO is negligible and does not constitute a step in the process of formation of the oxidised layer.
- The reversibility of the oxidation process decreases when the oxidation potential and the amount of the oxidised layer formed increase.
- EQCM and X-ray photoelectron spectroscopy experiments reveal the formation of significant amounts of $Co(OH)_2$ at oxidation potentials below −975 mV vs. Hg|HgO, while at potentials positive to this value CoO existence is detected.
- Three techniques (CV, CA and EQCM) reveal that below −880 mV vs. Hg|HgO, the oxidation of Co electrode follows a direct logarithmic law.
- An analysis of direct logarithmic law shows that at potentials not higher than −980 mV vs. Hg|HgO, the "electric field-assisted place exchange" model can correctly describe the oxidation process. At more positive potentials, this model does not correctly describe the influence of oxidation potential on the process in question. Further elucidation of the mechanism linked to the direct logarithmic law of growth of oxidised layers is required.

Acknowledgments This work was financially supported by the Ministry of Science and Higher Education (grant no. NN204 125037).

References

1. Alsabet M, Grdeń M, Jerkiewicz G (2006) J Electroanal Chem 589:120–127
2. Dall'Antonia LH, Tremiliosi-Filho G, Jerkiewicz G (2001) J Electroanal Chem 502:72-81
3. Tremiliosi-Filho G, Dall'Antonia LH, Jerkiewicz G (2005) J Electroanal Chem 578:1–8
4. Conway BE, Barnett B, Angerstein-Kozlowska H, Tilak BV (1990) J Chem Phys 93:8361–8373
5. Conway BE, Jerkiewicz G (1992) J Electroanal Chem 339:123–146
6. Gilroy D (1976) J Electroanal Chem 71:257–277
7. Alsabet M, Grdeń M, Jerkiewicz G (2011) Electrocatalysis 2:317–330
8. Chao CY, Lin LF, Macdonald DD (1981) J Electrochem Soc 128:1187–1194
9. Fromhold AT, Cook EL (1967) Phys Rev 163:650–664
10. Lawless KR (1974) Rep Prog Phys 37:231–316
11. Smeltzer WW, Young DJ (1975) Prog Solid State Chem 10:17–54
12. Tompkins HG, Augis JA (1981) Oxid Met 16:355–369
13. Łukaszewski M, Czerwiński A (2006) J Electroanal Chem 589:38–45
14. Łukaszewski M, Siwek H, Czerwiński A (2010) J Solid State Electrochem 14:1279–1292
15. Moyes RB, Roberts MW (1977) J Catal 49:216–224
16. Wohlfahrt-Mehrens M, Schenk J, Wilde PM, Abdelmula E, Axmann P, Garche J (2002) J Power Sources 105:182–188
17. Kleperis J, Wójcik G, Czerwiński A, Skowroński J, Kopczyk M, Bełtowska-Brzezińska M (2001) J Solid State Electrochem 5:229–249

18. Wang S (2006) JOM-J Min Met Mat Soc 58:47–50
19. Davis JR (2000) Nickel, cobalt, and their alloys. ASM, Materials Park
20. Ismail KM, Badawy WA (2000) J Appl Electrochem 30:1303–1311
21. Larramona G, Gutiérrez C (1990) J Electroanal Chem 293:237–252
22. Behl WK, Toni JE (1971) J Electroanal Chem 31:63–75
23. Burke LD, Lyons ME, Murphy OJ (1982) J Electroanal Chem 132:247–261
24. Jayaraman TR, Venkatesan VK, Udupa HVK (1975) Electrochim Acta 20:209–213
25. Sato N, Ohtsuka T (1978) J Electrochem Soc 125:1735–1740
26. Novoselsky IM, Menglisheva NR (1984) Electrochim Acta 29:21–27
27. Foelske A, Strehblow HH (2002) Surf Interface Anal 34:125–129
28. Göhr H, Krüger H (1966) Electrochim Acta 11:835–847
29. Foelske A, Kunze J, Strehblow HH (2004) Surf Sci 554:10–24
30. Santamaria M, Adragna E, Di Quarto F (2005) Electrochem Solid-State Lett 8:B12–B15
31. Cowling RD, Riddiford AC (1969) Electrochim Acta 14:981–989
32. Jung H, Alfantazi A (2010) Corrosion 66:035002–03500212
33. Erts D, Ahlberg E, Asbjörnsson J, Olin H, Prikulis J (1998) Appl Phys A—Mat Sci Process 66:S477–S480
34. Grdeń M, Klimek K, Rogulski Z (2009) Electrochem Commun 11:499–503
35. Gomez Meier H, Vilche JR, Arvia AJ (1982) J Electroanal Chem 134:251–272
36. Aledresse A, Alfantazi A (2004) J Mater Sci 39:1523–1526
37. Abd El Rehim SS, El Basosi AA, Osman MM (1993) J Electroanal Chem 348:99–106
38. Correia AN, Machado SAS, Avaca LA (1999) Electrochem Commun 1:600–604
39. Boukamp BA (1986) Solid State lonics 20:31–44
40. Pontinha M, Faty S, Walls MG, Ferreira MGS, Da Cunha Belo M (2006) Corr Sci 48:2971–2986
41. Elumalai P, Vasan HN, Munichandraiah N, Shivashankar SA (2002) J Appl Electrochem 32:1005–1010
42. Jukic A, Piljac J, Metikoš-Hukovic M (2001) J Mol Cat A - Chem 166:293–302
43. Sluyters-Rehbach M (1994) Pure Appl Chem 66:1831–1891
44. Brug GJ, Van Den Eeden ALG, Sluyters-Rehbach M, Sluyters JH (1984) J Electroanal Chem 176:275–295
45. Trasatti S, Petrii OA (1991) Pure Appl Chem 63:711–734
46. Nishizawa T, Ishida K (1983) Bull Alloy Phase Diagr 4:387–390
47. Koneshan S, Rasaiah JC, Lynden-Bell RM, Lee SH (1998) J Phys Chem B 102:4193–4204
48. Norkus E, Vaškelis A (1996) Electroanalysis 8:171–172
49. Ruetschi P, Amlie RF (1966) J Phys Chem 70:718–723
50. Pourbaix M (1966) Atlas of electrochemical equilibria in aqueous solutions. Pergamon, Oxford
51. Bard AJ (ed) (1975) Encyclopedia of electrochemistry of the elements, vol III. CRC, Boca Raton
52. Ohtsuka T, Sato N (1983) J Electroanal Chem 147:167–179
53. Thirsk HR, Harrison JA (1972) A guide to the study of electrode kinetics. Academic, London
54. Scharifker B, Hills G (1983) Electrochim Acta 28:879–889
55. Biesinger MC, Payne BP, Grosvenor AP, Lau LWM, Gerson AR, Smart RSC (2011) Appl Surf Sci 257:2717–2730
56. Gupta RP, Sen SK (1975) Phys Rev B 12:15–19
57. Yang J, Liu H, Martens WN, Frost RL (2010) J Phys Chem C 114:111–119
58. Kim KS (1975) Phys Rev B 11:2177–2185
59. Mclntyre NS, Cook MG (1975) Anal Chem 47:2208–2213
60. Casella IG, Guascito MR (1999) J Electroanal Chem 476:54–63
61. Pyun SI, Hong MH (1992) Electrochim Acta 37:327–332
62. MacDonald DD (2011) Electrochim Acta 56:1761–1772
63. Evans DH (2008) Chem Rev 108:2113–2144
64. Gileadi E (2002) J Electroanal Chem 532:181–189
65. Devanathan MAV (1972) Electrochim Acta 17:1683–1697
66. Armstrong RD, Harrison JA (1969) J Electrochem Soc 116:328–331